J. Phys. B: At. Mol. Opt. Phys. **32** (1999) 2629–2647. Printed in the UK PII: S0953-4075(99)99670-0

Multi-ion coincidence measurements of methyl chloride following photofragmentation near the chlorine K-edge

D L Hansen†, J Cotter‡, G R Fisher§, K T Leung‖, R Martin†, P Neill‡, R C C Perera§, M Simon¶[+], Y Uehara*, B Vanderford†, S B Whitfield[#] and D W Lindle†

† Department of Chemistry, University of Nevada, Las Vegas, NV 89154-4003, USA
‡ Department of Physics, University of Nevada, Reno, NV 89557-0058, USA
§ Lawrence Berkeley National Laboratory, Berkeley, CA 94720, USA
‖ Department of Chemistry, University of Waterloo, Canada, N2L 3G1
¶ LURE, Bâtiment 209D, Université Paris-Sud, 91405 Orsay Cedex, France
[+] CEA/DRECAM/SPAM, Bâtiment 522, CEN Saclay, 91191 Gif/Yvette Cedex, France
* Mitsubishi Electric Corporation, Amagasaki, Hyogo, 661 Japan
[#] Department of Physics and Astronomy, University of Wisconsin, Eau Claire, WI 54702, USA

Received 26 November 1998

Abstract. Relaxation dynamics of CH_3Cl following core-shell photoexcitation in the neighbourhood of the chlorine K-edge (≈ 2.8 keV) were studied via multi-ion coincidence measurements using a time-of-flight mass spectrometer. The data provide evidence for sequential fragmentation moderated by Coulombic interactions among the fragments. The sequential nature of the fragmentation indicates that chemical forces, especially between the carbon and chlorine atoms, are dominant in determining the kinematics of the fragmentation. This is especially true on resonance where fast dissociation is observed following electron excitations to the $8a_1$ antibonding orbital.

1. Introduction

Multi-ion coincidence techniques, often referred to as charge-separation mass spectroscopy (CSMS) [1], provide a powerful experimental tool for the determination of the dissociation dynamics of photoexcited molecules. Detection of several positively charged fragments from a single dissociation event allows differentiation among specific processes when a multitude of decay paths are possible, simplifying characterization of the photofragmentation mechanism. Synchrotron radiation (SR) is an excellent excitation source for these types of measurements, because it is readily made both tunable and monochromatic. Using x-ray SR, it is possible to excite a core electron localized around a specific atom in a molecule, providing a chemical-site-specific probe. By localizing the initially excited state, it is possible to determine whether site-selective-fragmentation effects, where the fragmentation pathways change as a result of excitation of electrons from chemically different sites, are present [2]. Both extremes for site selectivity exist, where either the decay pathway is dependent on the location of the initial excitation [3, 4], or where the system has no memory of the initially excited state [5, 6]. Studies of this type can find applications in biophysics, where dissociation of molecules following core-level excitation has been found to be a cause of radiation damage in biological tissues, as well

0953-4075/99/112629+19$19.50

as in astrophysics, where it helps to identify the interstellar photochemistry of dust and large hydrocarbon molecules [7].

The majority of coincidence studies have focused on photofragmentation dynamics of molecules following valence or shallow-core-level excitation, where a shallow-core level is defined as one in which a core hole (e.g. C $1s^{-1}$, Cl $2p^{-1}$) typically decays by interaction with one or more valence electrons. The sum of the charges on all fragments resulting from these interactions is usually +2 or less. In contrast, few studies [8] have used multi-ion-coincidence techniques to study the fragmentation dynamics of molecules following the formation of a deep-core-level hole (e.g. Cl $1s^{-1}$). Here a deep-core hole is one which can decay by first interacting with one or more shallow-core-level electrons. Decay of these deep-core holes often leads to highly charged residual ions (sums of charges on all fragments as high as +7 have been observed) due to their propensity to experience a stepwise series of decays known as a vacancy cascade [9–11]. The creation of highly charged ions in highly excited states can lead to the rupture of several bonds in a molecule, often leading to complete fragmentation. As a result, it is useful to perform multicoincidence measurements in order to gain a more complete picture of the fragmentation process.

In this work, an ion time-of-flight mass spectrometer and coincidence electronics were used to perform triple-coincidence CSMS measurements on CH_3Cl following photoexcitation of a Cl 1s electron by x-ray SR. Methyl chloride was studied for a number of reasons. Because of its relative simplicity as a singly substituted methane, an understanding of the fragmentation dynamics of CH_3Cl serves as a useful stepping stone toward understanding the fragmentation dynamics of more complex molecules, such as chlorofluorocarbons and their substitutes. Furthermore, comparison with similar previous studies of HCl [12, 13] allows differentiation of the kinematic changes that take place as the result of interchanging the hydrogen with a much heavier methyl radical. In addition, absorption measurements of CH_3Cl at the Cl K-edge [14] and ion time-of-flight measurements at the Cl L-edge [15] are available for comparison.

This paper will first discuss the SR source, the time-of-flight mass spectrometer, and the associated electronics used to perform the experiment. The results from the single-, double- and triple-coincidence measurements will be presented, and the triple-coincidence peaks will be analysed to determine their slopes. It will then be shown that the slopes of those peaks are consistent with a sequential fragmentation mechanism moderated by the Coulombic repulsion of the fragments. Because the fragmentation is primarily sequential, the kinematics of the fragmentation is mainly governed by the chemical forces between the carbon and chlorine atoms in the molecule. This point is further emphasized by an increase in the full width half maxima (FWHM) and therefore the fragmentation energy of the chlorine ions following resonant excitation. This additional energy, which is a result of the electrostatic repulsion following promotion of an electron into an antibonding orbital, causes the fragmentation mechanism to be more truly sequential on resonance.

2. Experimental

The experiments were performed using x-ray synchrotron radiation from beamline 9.3.1 at the Advanced Light Source (ALS) [16–18]. This beamline provides a flux of 10^{11} photons s^{-1} in a bandpass $\leqslant 0.5$ eV. The photon-energy calibration is checked periodically over the course of an experiment by scanning the monochromator through the Cl 1s threshold region (≈ 2.8 keV), while monitoring total ion yield (TIY) (figure 1). Because of the small probability ($<1\%$) for relaxation strictly through fluorescence [19], the total ion-yield spectrum obtained is in good agreement with previous absorption results [14]. The first peak in figure 1 is the result of Cl 1s

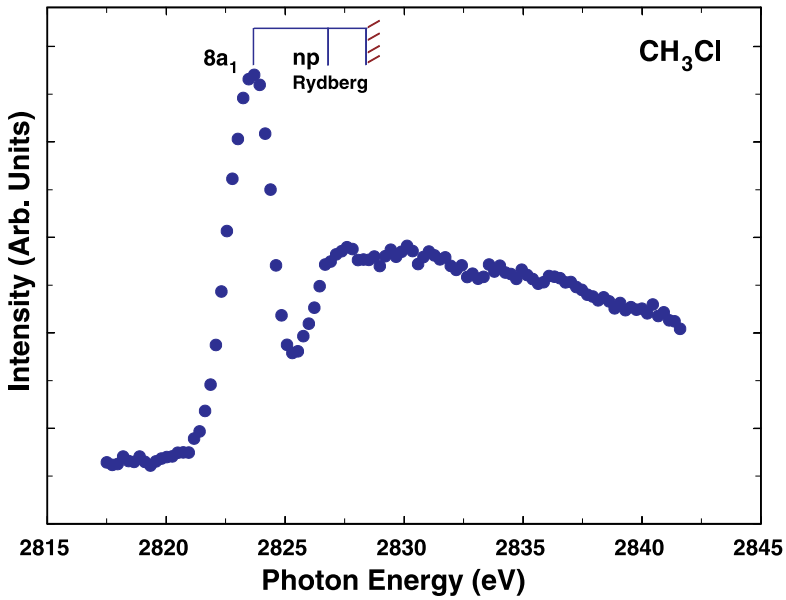

Figure 1. Total ion-yield spectrum of methyl chloride near the Cl K-edge.

($1a_1$) resonant excitation to the $8a_1$ antibonding molecular orbital. Rydberg excitations and the ionization threshold are also labelled.

An ion time-of-flight (TOF) mass spectrometer described previously [20], and oriented with its axis parallel to the polarization vector of the incident SR, was used to detect ions created following x-ray absorption. Briefly, the gas under study is supplied effusively by a grounded needle centred between two stainless-steel plates held at equal but opposite voltages. The ions created via x-ray absorption traverse a series of regions with different electric-field strengths until they are detected by a pair of microchannel plates.

For CH_3Cl, spectra were collected at photon energies in the vicinity of the K-shell ionization threshold with three levels of complexity. 'Singles' spectra were collected using an electronic set-up described previously [20]. A time-to-amplitude converter (TAC) measures the time difference between the detection of a single ion and the subsequent ring-timing pulse, thus flight times are inverted relative to the mass-to-charge ratio. Only one ion is detected for each fragmentation event and the data are recorded as the number of counts versus flight time. For 'doubles' and 'triples' spectra, a PC-based, multi-stop, time-to-digital converter (TDC) acts as a nanosecond stopwatch to record ion flight times. The ring timing signal is used to start the TDC, and detection of an ion is used to stop it. However, because the frequency of the ring-timing signal (≈ 3 MHz) is much greater than the ion count rate, it is necessary to use a logic circuit to reduce the amount of dead time from TDC starts with no corresponding stops. The set-up and timing diagram are shown in figure 2. For doubles and triples spectra, two or three ions are detected following a single fragmentation event; doubles data record flight times for two ions (t_1, t_2 counts), while triples data record flight times for three ions (t_1, t_2, t_3 counts).

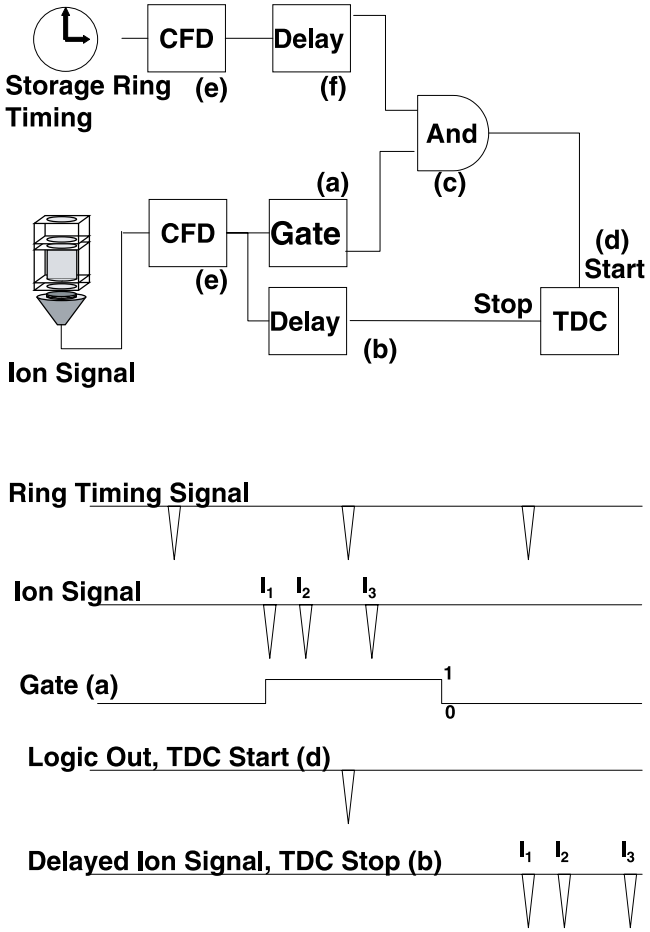

Figure 2. Set-up and timing diagram for the electronics used for double- and triple-ion-coincidence measurements. Following ion detection, the signal is split so one pulse triggers 'on' a gate generator (a) while the other is sent through a delay (b). The combination of the 'gate on' with the arrival of the subsequent ring timing pulse causes the 'and' gate (c) to output a start to the TDC (d). The delayed ion signal (b) then serves as the stop for the TDC. Constant fraction discriminators (e), which output a NIM logic pulse with timing independent of the amplitude of the input pulse, improve the timing characteristics of the signals, while the delay on the ring timing signal (f) adjusts the position of the spectra in the TDC window.

3. Results

Figure 3 shows singles spectra of CH_3Cl taken on and 8.4 eV above the $1a_1 \rightarrow 8a_1$ resonance. Because of the short period between pulses of the ALS when running in 'two-bunch' mode, ions 'wrap around' in the time window of the TAC, and thus do not appear in order of their charge-to-mass ratios. Peaks in the mass spectra are relatively straightforward to interpret because there are only three elements in CH_3Cl. In most cases, the mass differences among the fragments make it possible to resolve and unambiguously associate different ions with different peaks, the exception being $_{35}Cl^{3+}$ and C^+ ions which have $m/q = 11.66$ and $m/q = 12$, respectively.

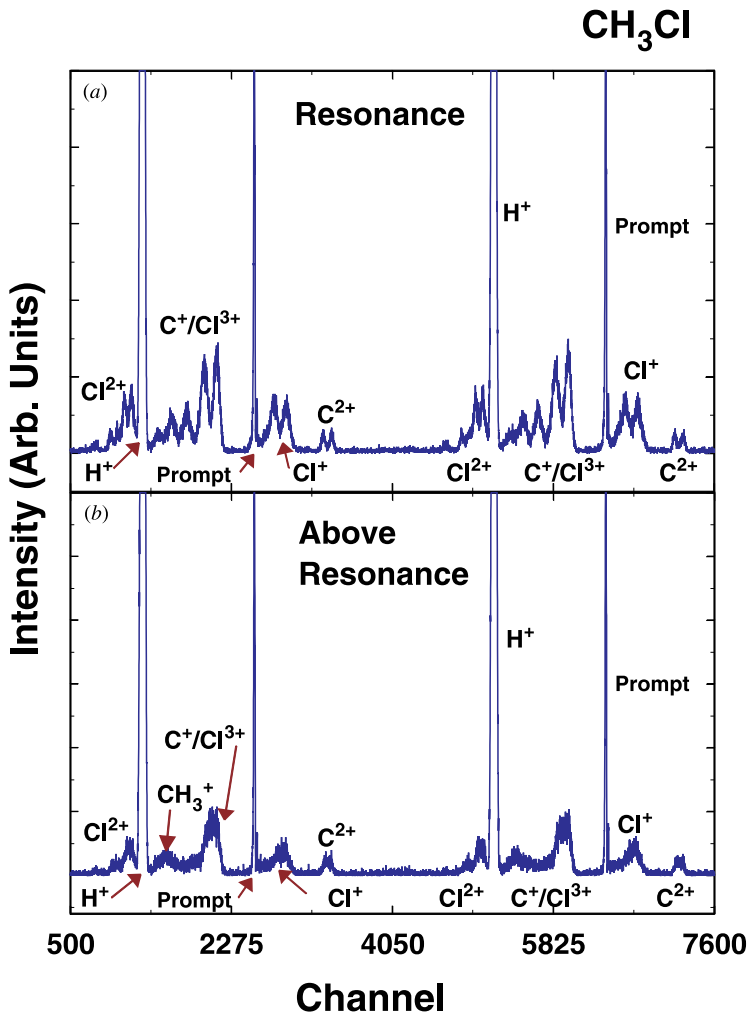

Figure 3. Singles spectra of CH_3Cl taken (*a*) on and (*b*) 8.4 eV above the $1a_1 \rightarrow 8a_1$ resonance. Because of the operation of the ALS in 'two-bunch' mode, two spectra are shown indicated by labels above or below the baseline. For the spectrum with labels above the baseline, the Cl^+ peak is wrapped around. For the spectrum with labels below the baseline the H^+ and prompt peaks are wrapped around. The prompt peak is the result of scattered light in the chamber.

The most notable difference between the on-resonance and above-resonance spectra in figure 3 is the splitting of the C^{m+} and Cl^{n+} peaks in the spectrum taken on resonance. Because of the well defined symmetry of the $8a_1$ excited orbital, molecules which have their axes aligned parallel to the polarization vector of the SR will preferentially absorb the incident photons. In CH_3Cl, the $8a_1$ orbital is analogous to the σ^* orbital in a diatomic molecule such as HCl [20], with much of its electron density along the C–Cl bond axis, but of course it maintains the C_{3v} symmetry of the molecule. Because fragmentation takes place rapidly relative to the rate of molecular rotation, and because the polarization vector of the SR is parallel to the axis of the

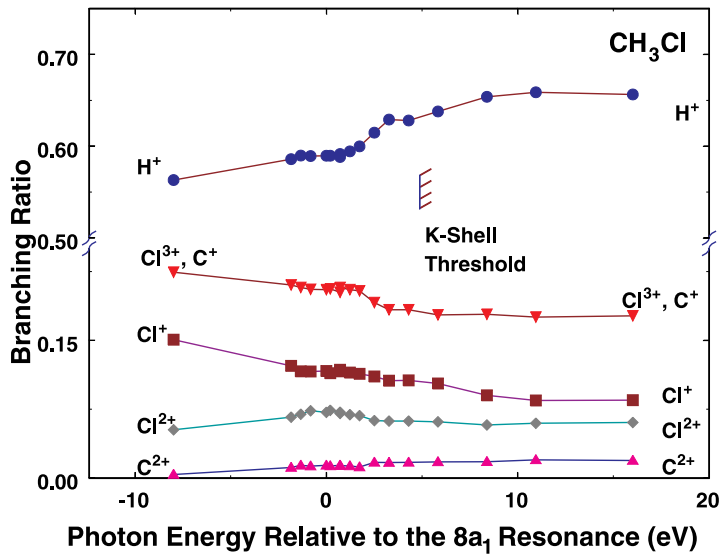

Figure 4. Fragment ion branching ratios as a function of energy for CH_3Cl singles spectra.

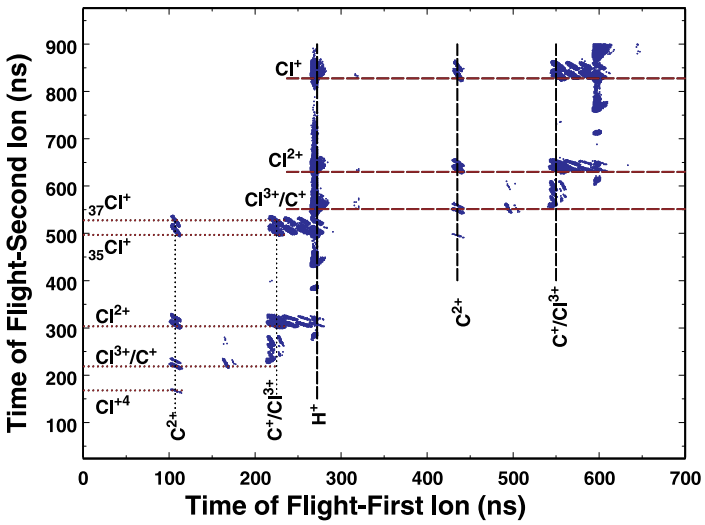

Figure 5. Double-coincidence spectrum for methyl chloride taken above threshold. The repeating structure is a result of two-bunch operation at the ALS. Dotted and broken lines denote coincident pairs.

analyser, the double peaks arise from ions ejected toward and away from the detector. The strength of these features indicates that on resonance, the asymmetry parameter β is positive, and probably approaches a value of 2 for the carbon and chlorine ions. This effect is in complete

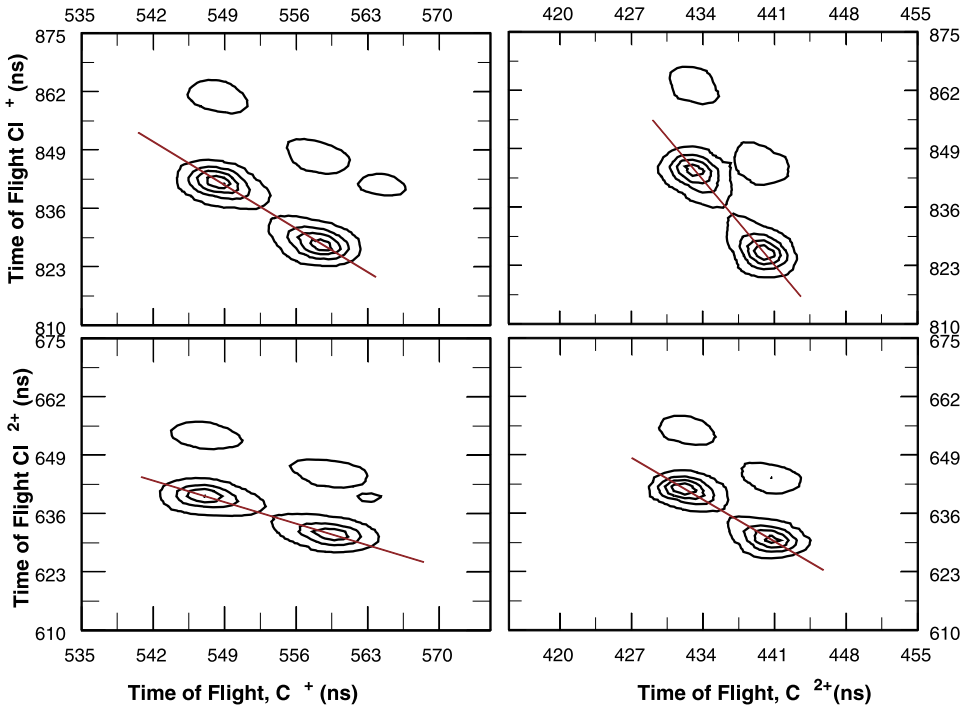

Figure 6. Coincidence peaks of the second and third ions of triple-coincidence events, where H^+ is the first ion detected, taken on the $1a_1 \rightarrow 8a_1$ resonance of CH_3Cl. Lines are drawn to indicate slopes. Flight times (in ns) for the second ion are on the x-axis, and flight times (in ns) for the third ion are on the y-axis.

analogy with the observed splitting of the H^+ peak following resonant excitation of HCl [20]. However, in the CH_3Cl case, the splitting is observed for the C^{m+} and Cl^{n+} peaks indicating that the C–Cl bond is aligned with the polarization vector of the SR rather than a C–H bond, as expected by the nature of the $8a_1$ antibonding orbital.

Peak areas from a number of singles TOF spectra taken at different photon energies were determined, yielding branching ratios of the different charge states in each spectrum (figure 4). The increase in the branching ratio for H^+ as a function of photon energy suggests that at higher energies (e.g. above threshold) the hydrogen atoms are less likely to fragment and remain neutral. The fact that three of the five atoms in CH_3Cl are hydrogens, would naively suggest a branching ratio for H^+ of 0.6. However, measured branching ratios depend on a number of factors, including the number of hydrogens fragmenting as neutrals; the collection efficiency of hydrogen as a function of fragmentation energy; and the detection efficiency of the MCPs. Because only the detection efficiency of the MCPs is well known, it is difficult to interpret the absolute values of the branching ratios, however, the relative change in the ratio can more reliably give information on the kinematic differences following excitation at different photon energies.

Figure 5 shows a double-coincidence spectrum for CH_3Cl taken above the ionization threshold. The x-axis gives the time of flight for the first ion detected in a coincident pair, while the y-axis gives the time of flight for the second ion detected. It is worthwhile noting several of the large-scale features of the spectrum. First, because the data were taken during

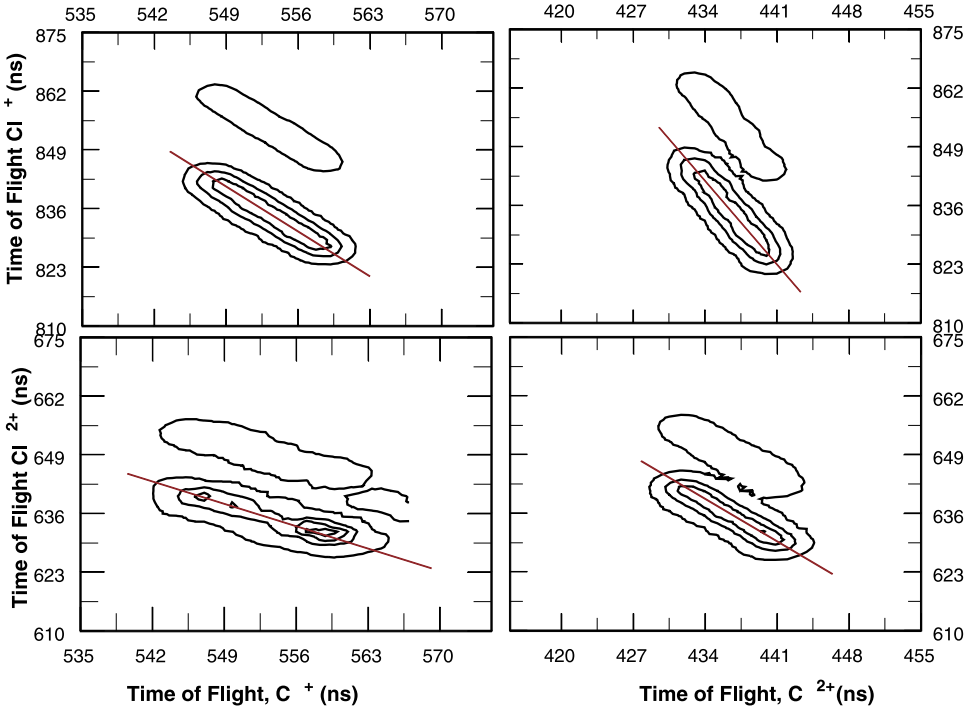

Figure 7. Coincidence peaks of the second and third ions of triple-coincidence events, where H^+ is the first ion detected, taken 60 eV above the $1a_1 \rightarrow 8a_1$ resonance of CH_3Cl. Lines are drawn to indicate slopes. Flight times (in ns) for the second ion are on the x-axis, and flight times (in ns) for the third ion are on the y-axis.

two-bunch mode at the ALS, the structure of the spectrum repeats itself for first-ion flight times greater than about 300 ns. Secondly, for first-ion flight times of about 100 ns, there is a series of peaks representing coincidences between C^{2+} ions and Cl^{n+} ions. These peaks come in pairs as a result of the two chlorine isotopes ($_{35}$Cl 75% and $_{37}$Cl 25%), and each pair has a different slope. Thirdly, for first-ion flight times of 220–270 ns there are two groups of peaks. These are a result of coincidences between either Cl^+ (second-ion flight time ≈ 500 ns) or Cl^{2+} (second-ion flight time ≈ 300 ns) and C^+, CH^+, CH_2^+ or CH_3^+. Finally, between the peaks representing CH_2^+–$_{35}Cl^+$ and CH_2^+–$_{37}Cl^+$ coincidences, it is possible to observe a small peak which represents coincidences between CH_2^+ and HCl^+. With sufficient statistics, it is also possible to observe coincidences involving H_2^+. These results indicate that rearrangement of atoms can occur during fragmentation. The fact that peaks from ions differing by 1 AMU can be distinguished gives a good indication of the resolution of the experiment.

Figures 6 and 7 show data taken in the triple-coincidence mode on resonance, and 60 eV above resonance, respectively. The x-axis represents the flight time of the second ion detected, while the y-axis represents the flight time of the third ion detected. Because these plots are of triple-coincidence data, each peak represents coincidences among H^+, C^{m+} and Cl^{n+} ions. In both figures as in the doubles spectrum, it is possible to observe coincidences with both chlorine isotopes. In addition, while the above-resonance plots (figure 7) show cigar-shaped contours, in the on-resonance spectra (figure 6), the contours are split into two round peaks. This is a further consequence of the alignment of the molecule by resonant excitation.

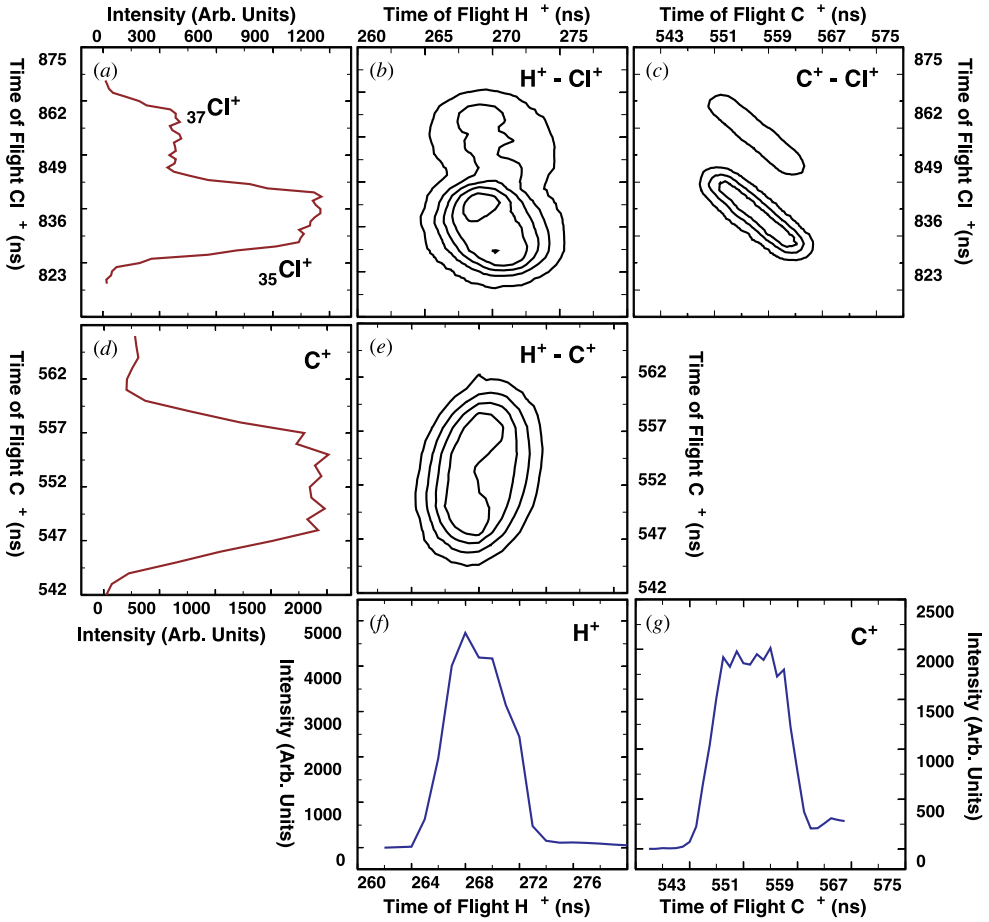

Figure 8. Projection of the coincidence triplet (H^+, C^+, Cl^+) taken 60 eV above resonance on to (*a*) the t_{Cl^+} axis; (*b*) the t_{H^+}, t_{Cl^+} plane; (*c*) the t_{C^+}, t_{Cl^+} plane; (*d*) and (*g*) the t_{C^+} axis; (*e*) the t_{H^+}, t_{C^+} plane and (f) the t_{H^+} axis. Two peaks resulting from the isotopes of chlorine are visible in (*a*)–(*c*).

Figure 8 shows data collected 60 eV above resonance for the coincidence triplet (H^+, C^+, Cl^+). In each figure, the three-dimensional coincidence volume defined by the flight times of the three ions detected (t_{H^+}, t_{C^+}, t_{Cl^+}) is projected into each of the planes (figures 8(*b*), (*c*) and (*e*)) and axes (figures 8(*a*), (*d*), (*f*) and (*g*)) defined by the flight times of the three ions. The projections of the coincidence volumes on to each of the planes give a plot similar to that shown for the double-coincidence spectra, while projections onto the TOF axes give a plot similar to that for the singles data.

4. Discussion

Because of the information it contains on the momentum released in the fragmentation process, the most important parameter in determining fragmentation mechanisms from multi-

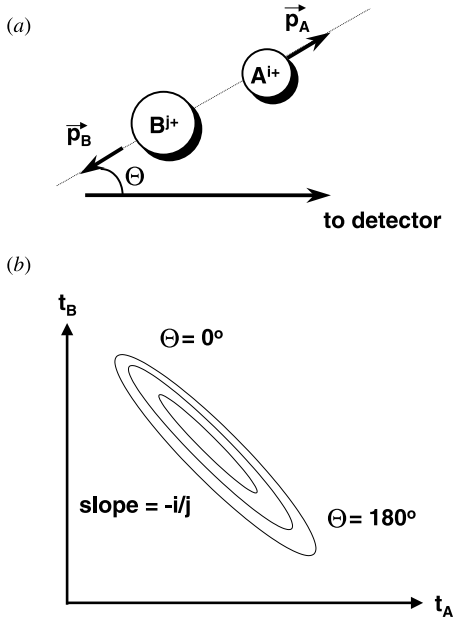

Figure 9. Schematic of the relevant fragmentation parameters involved in multi-coincidence measurements.

ion coincidence measurements is the slope of the coincidence peak [1]. The momentum p imparted to an ion during fragmentation can be related to the flight time of a detected ion by the expressions [21]

$$\text{TOF} = T^0 + \Delta t \tag{1}$$

and

$$\Delta t = \frac{kp}{q}\cos\Theta \tag{2}$$

where T^0, the flight time of an ion with no initial kinetic energy, is proportional to $(m/q)^{1/2}$, k is a constant which depends on the configuration of the analyser, q is the charge state and Θ is the angle between the bond axis and the analyser axis (figure 9(*a*)). In the simple case of a diatomic AB which fragments into A^{i+} and B^{j+}, fragment momenta will be anticorrelated ($p_A = -p_B$). If A^{i+} is the first ion detected, the coincidence map will show a cigar-shaped contour of slope $-i/j$ (figure 9(*b*)), with coincidences in the upper left-hand side of the contour produced by B^{j+} ions ejected away from the detector (extending the TOF for B^{j+}), and A^{i+} ions ejected toward the detector (reducing the TOF for A^{i+}). The opposite is true for coincidences in the lower right-hand corner of the contour plot.

Previous studies have enumerated mechanisms for three- [1, 22] and four-body [5] decay. For the sake of clarity, it useful to first look at mechanisms for three-body decay before extending the explanation to CH_3Cl. In fragmentation of a triatomic molecule ABC, we first look at the reaction sequence known as deferred charge separation (DCS), where a neutral

particle is ejected in the first step of dissociation, followed by charge separation:

$$\begin{aligned} &\mathrm{ABC}^{(i+j)+} \rightarrow \mathrm{AB}^{(i+j)+} + \mathrm{C} \ldots U_1 \\ &\mathrm{AB}^{(i+j)+} \rightarrow \mathrm{A}^{i+} + \mathrm{B}^{j+} \ldots U_2. \end{aligned} \tag{3}$$

Here, U_1 and U_2 are the energies released in each fragmentation step. If we can ignore U_1 relative to U_2, the momenta p_A and p_B will be anticorrelated ($p_\mathrm{A} = -p_\mathrm{B}$) and the coincidence contour will have a slope of $-i/j$ analogous to the two-body case (assuming A^{i+} is the first ion detected).

In another dissociation process known as secondary decay (SD), the detected fragments are ejected in different steps of the sequential dissociation

$$\begin{aligned} &\mathrm{ABC}^{(i+j)+} \rightarrow \mathrm{B}^{j+} + \mathrm{AC}^{i+} \ldots U_1 \\ &\mathrm{AC}^{i+} \rightarrow \mathrm{A}^{i+} + \mathrm{C} \ldots U_2. \end{aligned} \tag{4}$$

If U_2 is small compared to U_1, by conservation of momentum,

$$\begin{aligned} p_\mathrm{B} &= -p_\mathrm{AC} \\ p_\mathrm{A} &= \frac{m_\mathrm{A}}{m_\mathrm{A} + m_\mathrm{C}} p_\mathrm{AC} \\ &= \frac{-m_\mathrm{A}}{m_\mathrm{A} + m_\mathrm{C}} p_\mathrm{B} \end{aligned} \tag{5}$$

where p and m represent momentum and mass of a fragment. If A^{i+} is the first ion detected,

$$\text{slope} = \frac{\Delta t_\mathrm{B}}{\Delta t_\mathrm{A}} \tag{6}$$

$$= \frac{p_\mathrm{B}}{p_\mathrm{A}} \frac{i}{j} \tag{7}$$

$$= \frac{-(m_\mathrm{A} + m_\mathrm{C})}{m_\mathrm{A}} \frac{i}{j}. \tag{8}$$

Deferred charge separation and secondary decay mechanisms are valid in the case of clearly sequential steps, and typically produce contours with a parallelogram shape. In contrast, non-sequential or concerted dissociation (CD) processes

$$\mathrm{ABC}^{(i+j+k)+} \rightarrow \mathrm{A}^{i+} + \mathrm{B}^{j+} + \mathrm{C}^{k+} \ldots U_\mathrm{AB}, U_\mathrm{BC} \tag{9}$$

the distribution of energies among the fragments is not necessarily unique. The contours are frequently 'egg' shaped as a result of energy released by the ejection of the third fragment, with fragmentation events involving three ions generally having a larger momentum release than those involving dissociation of a neutral ion [23]. The 'cigar' shape of the contours in figure 7 suggests that this is not the primary mechanism of fragmentation for CH_3Cl.

Figure 10 gives slopes as a function of photon energy of the contours representing the projections of coincident volumes onto the (t_2, t_3)-plane (figure 8(*c*)). Slopes were determined through inspection of the contour diagrams. Because of uncertainties in flight times and, in some cases, the asymmetry of the peaks, this is considered the most reliable method for determining slopes [23, 24]. Dotted lines in figure 10 represent values for the slope calculated using the SD mechanism (equation (8)) for dissociation, with the first step being the rupture of the C–Cl bond and the second step the rupture of all three C–H bonds assuming no energy is released on breaking the C–H bonds. Modelling fragmentation using the DCS mechanism, results for all the ion pairs in figure 10 are either outside the error bars of the measured data or do not agree with the data as well as the values calculated using the SD mechanism. The good agreement between the measured and calculated slopes for the ion pairs and the fact that

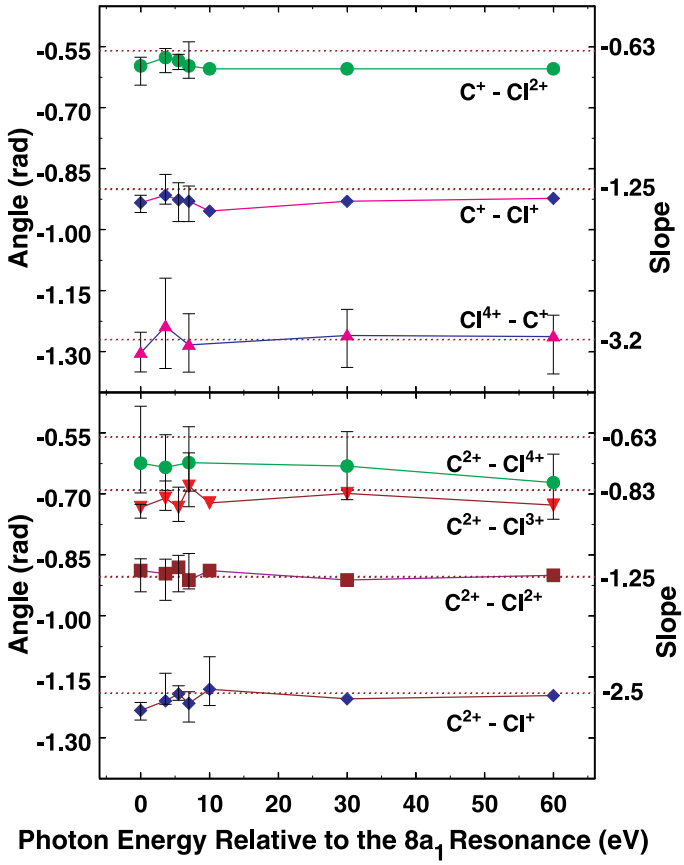

Figure 10. Slopes of the contour plots representing the second and third ions detected in triples mode as a function of photon energy. Dotted lines represent calculated values assuming a secondary-decay mechanism (see text).

fluctuations in the slopes as a function of energy are within the error bars indicates that the SD mechanism describes the fragmentation process across the photon-energy range studied to a good approximation. This underscores the importance of the chemical forces in determining the dissociation dynamics of CH_3Cl. If the Coulombic repulsion dominated the dissociation, the fragmentation mechanism would not be sequential but concerted.

If no energy is released in the second step of the fragmentation process (i.e. rupture of all three C–H bonds), as assumed in calculating the dotted lines in figure 10, then H^+ and C^{i+} will share the momentum released in the rupture of the C–Cl bond according to the ratio of their masses. Using the same reasoning that yielded equation (5), the slopes of the H^+–C^{i+} contours would be given by $m_C/(m_H i) = 12/i$, and the slopes of the H^+–Cl^{j+} contours would be given by $-m_{CH_3}/(m_H j) = -15/j$. Figures 11 and 12 show that this is not the case, at least for more highly charged fragmentation channels. In addition, the oval shapes of the H^+–C^{i+} (e.g. figure 8(*e*)) and H^+–Cl^{j+} (e.g. figure 8(*b*)) contours suggest that the kinetic energy released in the fragmentation of an H^+ ion is not negligible.

There are two competing effects which can cause deviant slopes within the model of

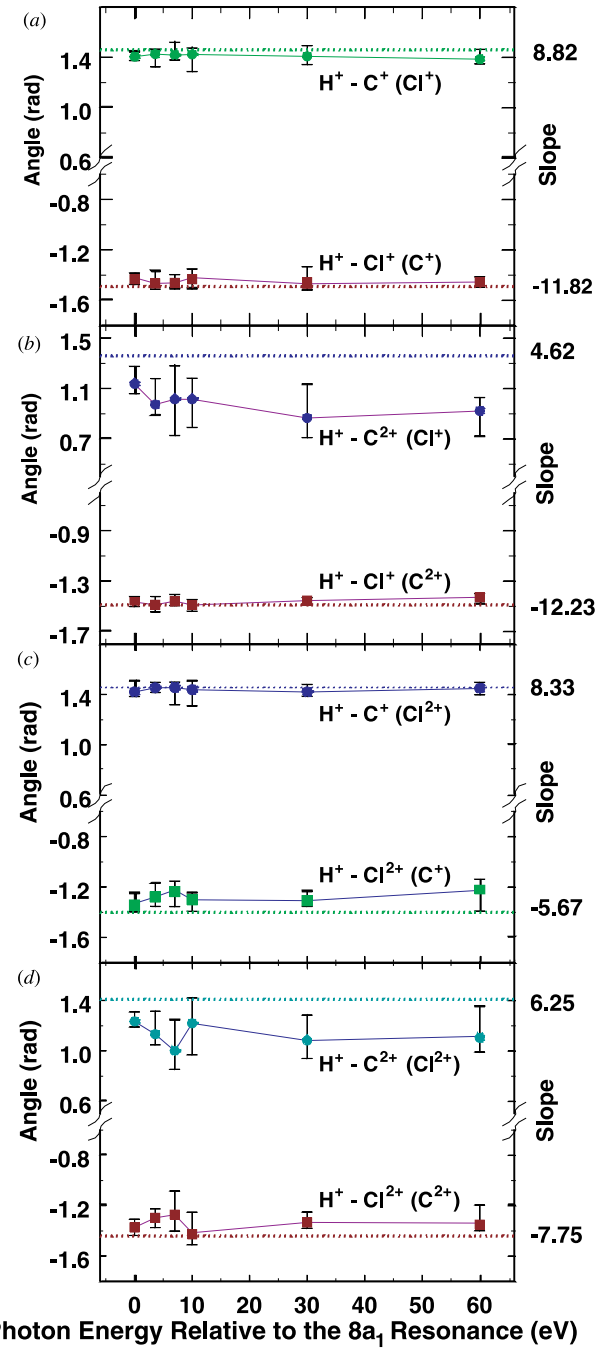

Figure 11. Slopes of coincidence contours for two ions of a coincident triplet. For example, the top plot in (*a*) gives the slopes of the contours for H^+ and C^+ measured in coincidence with Cl^+, while the bottom plot in (*a*) gives the slopes of the coincidence contours for H^+ and Cl^+ measured in coincidence with C^+. Dotted lines represent the calculated values of slope assuming a secondary-decay mechanism (see text).

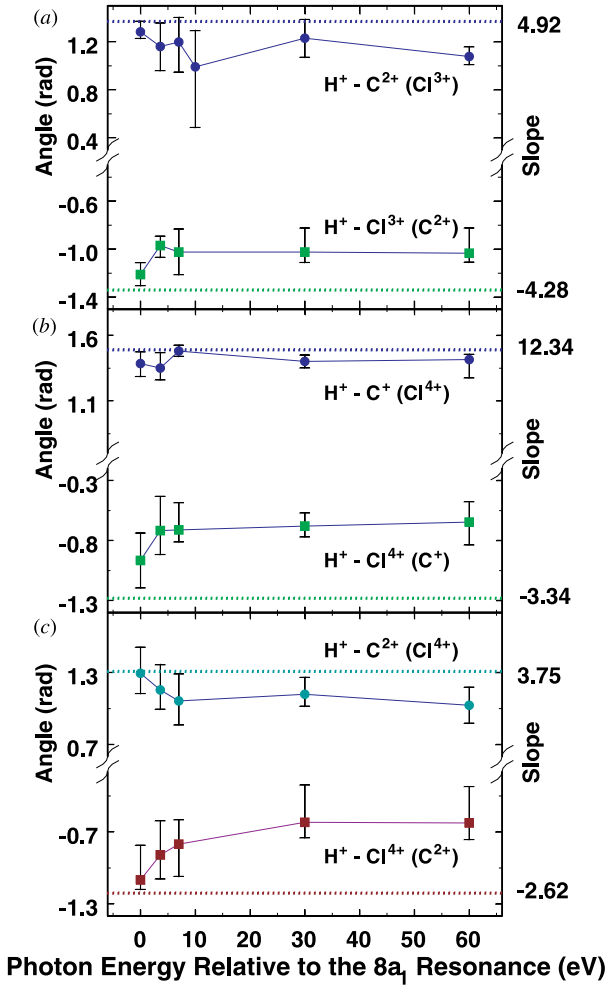

Figure 12. Slopes of the coincidence contours for two ions of a coincident triplet. See the previous figure for further explanation. Dotted lines represent the calculated values of slope assuming a secondary-decay mechanism (see text). Because the difference between the mass-to-charge ratios for C^+ and Cl^{3+} is too small for the analyser to resolve, no data are shown for the coincident triplet H^+, C^+, Cl^{3+}.

secondary decay [24]. In the first, the lifetime of the intermediate molecule is sufficiently short that it dissociates within the Coulomb field of the first fragment. The additional repulsion between the charged particles causes the two detected ions to have more strongly anticorrelated momenta, moving the peak slope nearer to $-i/j$, where the ion with charge i is detected before the ion with charge j. The second explanation for deviant slopes is a release of momentum in the second dissociation step. Only cases where the momentum released in the second step is aligned with the momentum released in the first step will lead to changes in slope. In order for this to occur, the second step must take place on a time scale which is shorter than that for rotation of the intermediate. Because it requires a short time scale for dissociation, it is

likely that the secondary step will take place within the range of the Coulomb repulsion of the first fragment. Thus these two effects are not completely separable. This is especially true following photoexcitation of an electron in a deep-core level such as Cl 1s because of the short lifetime of the core hole (1.1 fs), and the high ionic charge states seen as a result of molecular relaxation through Auger vacancy cascades.

Generalization of the SD fragmentation mechanism to the case of CH_3Cl, taking into account the energy released in both fragmentation steps, can be done in the following manner. Keeping in mind that the energy released is shared among five particles,

$$p_{\mathrm{Cl}}^2 = \frac{2U_1(m_{\mathrm{Cl}}m_{\mathrm{CH_3}})}{m_{\mathrm{CH_3Cl}}} \tag{10}$$

and

$$q_{\mathrm{HC}}^2 = \frac{2U_2(m_{\mathrm{H}}m_{\mathrm{C}})}{m_{\mathrm{CH}}} \tag{11}$$

where $\boldsymbol{p}_{\mathrm{Cl}}$ represents the momentum of the Cl^{n+} ion, U_1 represents the energy released in the rupture of the C–Cl bond, m represents the mass of individual fragments, and U_2 and $\boldsymbol{q}_{\mathrm{HC}}$ are the energy and momentum released by the breaking of one H–C bond in the second fragmentation step. The expression for $\boldsymbol{q}_{\mathrm{HC}}$ assumes that all three H^+ bonds rupture simultaneously and that each hydrogen is pushing only against the carbon ion along the C–H bond axis. Combining the effects of both fragmentation steps yields

$$\boldsymbol{p}_{\mathrm{C}} = \sum_{i=1}^{3} \boldsymbol{q}_{\mathrm{HC}i} - \frac{m_{\mathrm{C}}}{m_{\mathrm{CH_3}}}\boldsymbol{p}_{\mathrm{Cl}} \tag{12}$$

and

$$\boldsymbol{p}_{\mathrm{H}} = -\boldsymbol{q}_{\mathrm{HC}} - \frac{m_{\mathrm{H}}}{m_{\mathrm{CH_3}}}\boldsymbol{p}_{\mathrm{Cl}} \tag{13}$$

where the summation represents the contribution from all three hydrogens to the momentum of the C^{m+} ion.

Equations (12) and (13) can be used to predict ratios of momenta and thus slopes of coincidence contours. In order to do this, only momenta parallel to the analyser axis are relevant. Choosing the z-axis as parallel to the axis of the analyser and assuming all three hydrogens function identically yields

$$\boldsymbol{p}_{\mathrm{C}z} = \left[3\cos\theta\left(\frac{2U_2 m_{\mathrm{H}} m_{\mathrm{C}}}{m_{\mathrm{CH}}}\right)^{1/2} - \frac{m_{\mathrm{C}}}{m_{\mathrm{CH_3}}}\left(\frac{2U_1\, m_{\mathrm{Cl}}\, m_{\mathrm{CH_3}}}{m_{\mathrm{CH_3Cl}}}\right)^{1/2}\right]\hat{z} \tag{14}$$

and

$$\boldsymbol{p}_{\mathrm{H}z} = \left[-\cos\theta\left(\frac{2U_2 m_{\mathrm{H}} m_{\mathrm{C}}}{m_{\mathrm{CH}}}\right)^{1/2} - \frac{m_{\mathrm{H}}}{m_{\mathrm{CH_3}}}\left(\frac{2U_1 m_{\mathrm{Cl}} m_{\mathrm{CH_3}}}{m_{\mathrm{CH_3Cl}}}\right)^{1/2}\right]\hat{z} \tag{15}$$

where θ is the angle between a C–H bond and the C–Cl bond axis. Equations (10), (12) and (13) can be combined to obtain the ratios:

$$\frac{p_{\mathrm{Cl}}}{p_{\mathrm{C}}} = \left[3\cos\theta\left(\frac{U_2}{U_1}\right)^{1/2}\left(\frac{m_{\mathrm{H}} m_{\mathrm{C}} m_{\mathrm{CH_3Cl}}}{m_{\mathrm{Cl}} m_{\mathrm{CH_3}} m_{\mathrm{CH}}}\right)^{1/2} - \frac{m_{\mathrm{C}}}{m_{\mathrm{CH_3}}}\right]^{-1} \tag{16}$$

$$\frac{p_{\mathrm{Cl}}}{p_{\mathrm{H}}} = \left[-\cos\theta\left(\frac{U_2}{U_1}\right)^{1/2}\left(\frac{m_{\mathrm{H}} m_{\mathrm{C}} m_{\mathrm{CH_3Cl}}}{m_{\mathrm{Cl}} m_{\mathrm{CH_3}} m_{\mathrm{CH}}}\right)^{1/2} - \frac{m_{\mathrm{H}}}{m_{\mathrm{CH_3}}}\right]^{-1} \tag{17}$$

and

$$\frac{p_C}{p_H} = \left[3\cos\theta\left(\frac{U_2}{U_1}\right)^{1/2}\left(\frac{m_H m_C}{m_{CH}}\right)^{1/2} - \frac{m_C}{m_{CH_3}}\left(\frac{m_{Cl}m_{CH_3}}{m_{CH_3Cl}}\right)^{1/2}\right] \times \left[-\cos\theta\left(\frac{U_2}{U_1}\right)^{1/2}\left(\frac{m_H m_C}{m_{CH}}\right)^{1/2} - \frac{m_H}{m_{CH_3}}\left(\frac{m_{Cl}m_{CH_3}}{m_{CH_3Cl}}\right)^{1/2}\right]^{-1}. \quad (18)$$

Naturally, if $U_2 \ll U_1$ these expressions reduce to equation (8).

Because the slopes of contours for the second and third ions were nearly constant, within experimental error over the energy range studied, the average of the measured values shown in figure 10 has been used along with equation (16) to determine a value for the term $\cos\theta\,(U_2/U_1)^{1/2}$. Using these values in equations (17) and (18), slopes for the H^+–C^{m+} (e.g. figure 8(*e*)) and H^+–Cl^{n+} (e.g. figure 8(*b*)) contours were determined. The calculated slopes are shown as dotted lines in figures 11 and 12. Finally, using a similar procedure to take into account the kinetic energy released in both dissociation steps but using the deferred charge-separation mechanism instead of the secondary-decay mechanism produced a negative value for $(U_2/U_1)^{1/2}$, providing further evidence for the SD mechanism.

The most notable trend in figures 11 and 12 is the agreement between the experimental values and the calculated values decreases as the ionic charge increases. The slopes of the Cl^+ contours (figures 11(*a*) and (*b*)) show good agreement between the data and the calculated values. However, for the slopes of the Cl^{2+} contours (figures 11(*c*) and (*d*)), a slight deviation toward less negative slopes relative to the calculated values is observed. The trend continues for the Cl^{3+} contour (figure 12(*a*)) and the Cl^{4+} contours (figures 12(*b*) and (*c*)), with Cl^{4+} showing the greatest deviation from the calculated slope. However, when comparing the slopes of identical chlorine charge states in coincidence with different carbon charge states, agreement between the slopes and the calculated values is very similar. For example, the slopes of the contours representing H^+–Cl^+ in coincidence with C^+ (figure 11(*a*)) and H^+–Cl^+ in coincidence with C^{2+} (figure 11(*b*)) are both in good agreement with the calculated values. Similarly, the slopes of the contours representing H^+–Cl^{4+} in coincidence with C^+ (figure 12(*b*)) and H^+–Cl^{4+} in coincidence with C^{2+} (figure 12(*c*)) both deviate from the calculated values by about the same amount. The same trends hold true for the carbon ions; uniformly, the C^+ ions agree with the calculated values (figures 11(*a*), (*c*), 12(*b*)), whereas the C^{2+} results deviate from the calculated values (figures 11(*b*), (*d*), 12(*a*), (*c*)).

These observations can be explained by the greater Coulombic interaction between an ion and its neighbours as the charge state increases. Because of the interaction, there is a more even sharing of the momentum released in fragmentation. The fragmentation is not purely sequential and there is a shift of the slope toward $-1/n$, where n is the charge on the ion measured in coincidence with H^+. For further confirmation of this explanation, it is instructive to look at the FWHM of the coincidence peaks. This was determined for each ion by projecting the coincidence volume on to the appropriate axis (e.g. figures 8(*a*), (*d*), (*f*) and (*g*)), and then determining the energy released in fragmentation (U_0) using the expression [21]

$$U_0 = \left(\tfrac{1}{2}qEt\right)^2 \frac{1}{2m} \quad (19)$$

where q, E, t and m are the charge, electric field in the interaction region, peak width and mass of the ion, respectively. The average FWHM for all photon energies are shown as a function of chlorine charge state in figure 13. These results show that increasing the chlorine charge state increases the peak width for both the chlorine ion as well as the carbon ion detected in coincidence with it. The same can be said about increasing the charge state of the carbon ion. Thus the data show that the energy released in fragmentation increases with an increase

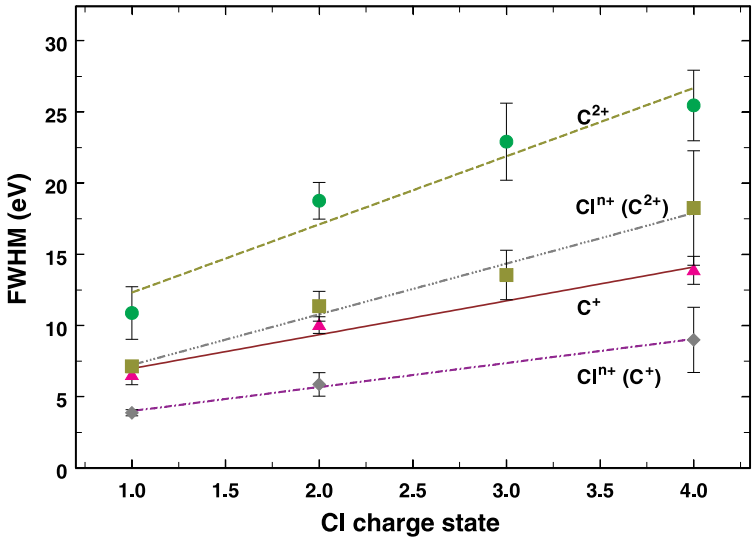

Figure 13. Average FWHM for all photon energies plotted as a function of chlorine charge state. ●, FWHM of a C^{2+} ion measured in coincidence with a H^+ and Cl^{n+} ion; ■, FWHM of a Cl^{n+} ion measured in coincidence with a H^+ and C^{2+}; ▲, FWHM of a C^+ ion measured in coincidence with a H^+ and Cl^{n+} ion; ♦, FWHM of a Cl^{n+} ion measured in coincidence with a H^+ and C^+ ion. Lines represent a linear fit to the data.

in the total charge of the detected fragments, providing additional evidence that an increased Coulombic interaction must be taken into account in describing fragmentation mechanisms for highly charged species.

Figures 11(*a*)–(*c*) show that for the singly charged ions (C^+, Cl^+) measured in coincidence with H^+ there appears to be little or no change in slope, and thus mechanism, as a function of energy. However, the situation is different for more highly charged ions. The slopes of the H^+–Cl^{3+} (figure 12(*a*)) and H^+–Cl^{4+} (figures 12(*b*) and (*c*)) peaks clearly change in the first few eV above resonance, and show better agreement with the calculated values on resonance. Looking at the widths of the chlorine peaks as a function of energy (figure 14) indicates that for all charge states, there is a greater amount of energy released in fragmentation on resonance than at energies above resonance. A likely explanation for this is that on resonance, the excitation of the core electron into the $8a_1$ antibonding orbital initiates the C–Cl bond rupture, consequently, the electrostatic repulsion introduced by population of an antibonding orbital causes a more energetic ejection of the chlorine ion in a manner analogous to the fast dissociation observed for resonant excitation of HCl [12]. Because of this, the chlorine ion has less Coulombic interaction with the other ions, the fragmentation is more sequential, and the slopes of the coincidence peaks show better agreement with the values calculated using the sequential model. In addition, for all ionic triplets, the FWHM for the H^+ ions (not shown) are consistently narrower on resonance, as would be expected in the case of a reduced Coulombic interaction.

In contrast, on excitation to the Rydberg orbitals (3.4 eV above resonance) or to the continuum (5 eV above resonance), rupture of the C–Cl bond results solely from electronic depletion following Auger decay. In addition, with the higher ionic charge states

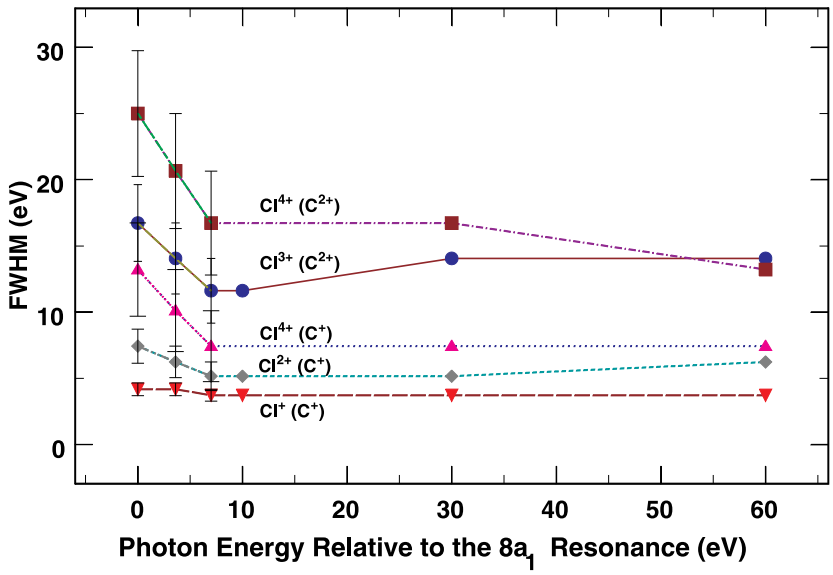

Figure 14. FWHM of chlorine ion peaks versus photon energy. ■, FWHM of Cl^{4+} measured in coincidence with H^+ and C^{2+}; ●, FWHM of Cl^{3+} measured in coincidence with H^+ and C^{2+}; ▲, FWHM of Cl^{4+} measured in coincidence with H^+ and C^+; ♦, FWHM of Cl^{2+} measured in coincidence with H^+ and C^+; ▼, FWHM of Cl^+ measured in coincidence with H^+ and C^+.

inherent to above-threshold energies comes greater mutual repulsion between the ions making fragmentation a more concerted process and bringing the slope closer to $-1/i$ for a C^{i+} ion or $-1/j$ for a Cl^{j+} ion plotted in coincidence with H^+. These results suggest that by using multi-ion-coincidence techniques it is possible, in principle, to determine an upper bound for the energy of the electrostatic repulsion arising from excitations to the $8a_1$ antibonding orbital, and to use this information to map out the potential curves for different fragmentation pathways. However, because a large extraction voltage was used in these experiments, the resolution for the kinetic energy of the fragments is poor, and it is difficult to derive any quantitative conclusions.

5. Conclusion

In conclusion, the fragmentation dynamics of CH_3Cl were studied using triple-coincidence CSMS methods. By measuring the slopes of different coincidence maps, and looking at the FWHM of the different ions, it is found that a sequential decay mechanism, initiated by the rupture of the C–Cl bond, describes the dissociation process well for all ionic charge states, and that the process is moderated by Coulombic interaction among the particles. In addition, an increase in the FWHM on resonance, combined with better agreement of the slopes of the more highly charged chlorine ions with the calculated values, was attributed to fast dissociation caused by the electrostatic repulsion following excitation of a core electron to the $8a_1$ antibonding orbital. The sequential dissociation as well as the additional electrostatic repulsion following resonant excitation provide strong evidence that chemical forces are the

dominant factor governing the kinematics of the fragmentation, and that Coulombic repulsion plays a subordinate role in the dissociation.

Acknowledgments

The authors thank the staff of the ALS for their excellent support. Support from NSF, Nevada DOE EPSCoR, Research Corporation, The Petroleum Research Fund, NATO and the UNLV Sabbatical Leave Committee is gratefully acknowledged. This work was performed at the Advanced Light Source, supported by DOE (DE-AC03-76SF00098).

References

[1] Eland J H D 1989 *Acc. Chem. Res.* **22** 381
[2] Nenner I, Reynaud C, Schmelz H C, Ferrand-Tanaka L, Simon M and Morin P 1996 *Z. Phys. Chem.* **195** 43
[3] LeBrun T, Lavollée M, Simon M and Morin P 1993 *J. Chem. Phys.* **98** 2534
[4] Simon M, Lavollée M, Meyer M and Morin P 1996 *J. Electron Spectrosc. Relat. Phenom.* **79** 401
[5] Simon M, Lebrun T, Martins R, de Souza G G B, Nenner I, Lavollee M and Morin P 1993 *J. Phys. Chem.* **97** 5228
[6] Simon M, Lavollée M, Morin P and Nenner I 1995 *J. Phys. Chem.* **99** 1733
[7] Nenner I and Morin P 1996 *VUV and Soft X-ray Photoionization* ed U Becker and D A Shirley (New York: Plenum) p 291
[8] Ankerhold U, Esser B and von Busch F 1997 *J. Phys. B: At. Mol. Opt. Phys.* **30** 1207
[9] Carlson T A and Krause M O 1965 *Phys. Rev.* **137** 1655
[10] Carlson T A, Hunt W E and Krause M O 1966 *Phys. Rev.* **151** 41
[11] Krause M O and Carlson T A 1967 *Phys. Rev.* **158** 18
[12] Hansen D L *et al* 1998 *Phys. Rev.* A **57** 2608
[13] Hansen D L *et al* 1998 *Phys. Rev.* A **57** R4090
[14] Lindle D W, Cowan P L, Jach T, LaVilla R E, Deslattes R D and Perera R C C 1991 *Phys. Rev.* A **43** 2353
[15] Thissen R, Simon M and Hubin-Franskin M-J 1994 *J. Chem. Phys.* **101** 7548
[16] Jones G, Ryce S, Lindle D W, Karlin B A, Woicik J C and Perera R C C 1995 *Rev. Sci. Instrum.* **66** 1748
[17] Perera R C C, Jones G and Lindle D W 1995 *Rev. Sci. Instrum.* **66** 1745
[18] Ng W, Jones G, Perera R C C, Hansen D, Daniels J, Hemmers O, Glans P, Whitfield S, Wang H and Lindle D W 1996 *Rev. Sci. Instrum.* **67** 1
[19] Krause M O 1979 *J. Phys. Chem. Ref. Data* **8** 307
[20] Hansen D L *et al* 1998 *Phys. Rev.* A **58** 3757
[21] Wiley W C and McLaren I H 1955 *Rev. Sci. Instrum.* **26** 1150
[22] Eland J H D 1987 *Mol. Phys.* **61** 725
[23] Eland J H D and Treves-Brown B J 1992 *Conf. Proc. Synchrotron Radiation and Dynamic Phenomena (Grenoble)* (*AIP* vol 258) ed A Beswick (New York: AIP) p 100
[24] Eland J H D 1993 *Chem. Phys. Lett.* **203** 353